Physics potential of LHC

Contribution to Proceedings of TEA03 (Oct. 2003)

S. Asai

Abstract

This document describes the physics potential of LHC. There are many topics covered at LHC from low p_T physics to new physics beyond the standard model, high mass and high transverse momentum physics are main purpose of LHC. This note is focused on two major topics, Higgs boson(s) and Supersymmetry. ATLAS and CMS collaborations have enormous potential to discover Higgs boson(s) and Supersymmetry within one year, if it exists at mass scale less than about 1 and 2 TeV, respectively.

ICEPP

International Center for Elementary Particle Physics,
University of Tokyo
7-3-1 Hongo, Bunkyo-ku, Tokyo 113-0033, Japan

1 Introduction

The Large Hadron Collider(LHC) project [1] is the major accelerator program at CERN, and it is now under contraction using the existing 26.6 km circumference LEP tunnel. 1234 units of 8.4 T superconducting dipole magnet (length of the magnetic field is 14.2 m each) will be arranged in the tunnel with 392 units of the quadruple magnet. Protons are accelerated up-to 7 TeV and collide each other, and the centre-of-mass energy of pp-system is 14 TeV. The pilot run is scheduled in July 2007, and the first physics run will start in autumn 2007. Although the design luminosity is $10^{34} cm^{-2} s^{-1}$, LHC will be operated with the lower luminosity of about $10^{33} cm^{-2} s^{-1}$ during the first year run, and a luminosity of 10 fb^{-1} will be integrated within this year. LHC has an excellent performance to discover Higgs and Supersymmetry with the data of the only 10 fb^{-1} taken in the first year. In this note, the discovery potential of these particles are summarized.

Two general-purpose experiments exist, ATLAS [2] and CMS [3], at LHC. The ATLAS (A Toroidal LHC Apparatus) detector is illustrated in Fig. 1, and it measures 22 m high, 44 m long, and weight 7,000 tons. The characteristics of the ATLAS detector are summarized as follows [4]:

- Precision inner tracking system is constituted with pixel, strip of silicon and TRT with 2 T solenoidal magnet. Good performance is expected on the B-tagging and the γ-conversion tagging.

- Liquid Argon electromagnetic calorimeter has fine granularity for space resolution and longitudinal segmentation for fine angular resolution and particle identifications. It has also good energy resolution of about 1.5% for e/γ with energy of 100 GeV.

- Large muon spectrometer with air core toroidal magnet will provide a precise measurement on muon momenta(about 2% for 100 GeV-μ) even in the forward region.

The CMS (Compact Muon Solenoid) detector measures 15 m high, 21 m long, and weight 12,500 tons, with the following features [5]:

- Precise measurement on high p_T track is performed with the strong 4 T solenoidal magnet.

- P$bW0_4$ crystal electromagnetic calorimeter is dedicated for $H^0_{SM} \rightarrow \gamma\gamma$.

- High purity identification and precise measurement are expected on μ tracks using the compact muon system.

The production cross-sections are expected to be huge at LHC for the various high p_T and high mass elementary processes, since gluon can contribute remarkably even to such processes. Furthermore, LHC provides the high luminosity, and the large numbers of the interesting events will be observed as summarized in table 1. LHC has an enormous potential to produce the high mass particles, for example, top quark, Higgs boson and SUSY particles.

2 Higgs physics

The most urgent and important issue of the elementary particle physics is to understand the mechanism of the Electroweak symmetry-braking and origin of mass. Four experiments at LEP have shown very precisely the validity of the Standard model(SM) for the last 10 years. But there is still the missing knowledge about the Electroweak symmetry-braking, which is crucial for the Standard model. The experimental observation of one or several Higgs bosons will give a solution to this important issue. Furthermore, the detail studies on Yukawa couplings between
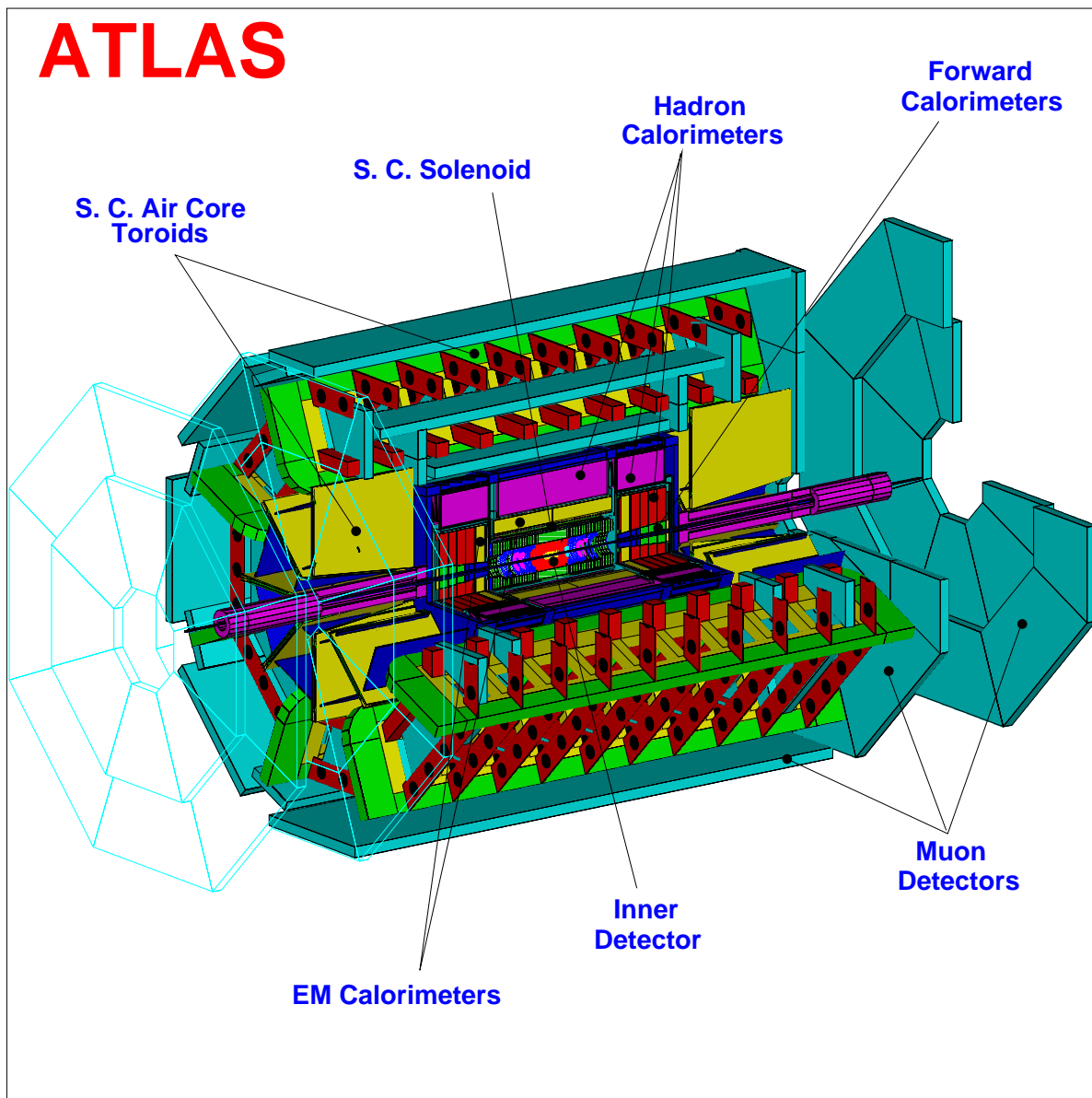
Figure 1: Overall layout of the ATLAS (A Toroidal LHC Apparatus) detector.

Table 1: Event rates for major high p_T and high mass processes with a luminosity of $10\text{fb}^{-1}/\text{year}$. The expected numbers of events observed at Tevatron Run-II and Belle until 2007 are also listed, for the comparison.

Process	Rate (Hz)	Event number at LHC (First one year)	Comparing to the others (Integrated numbers until 2007)
$W^{\pm} \to e^{\pm}\nu$	15	10^8	10^7 Tevatron-II
$Z^0 \to e^+e^-$	1.5	10^7	10^7 Tevatron-II
$t\bar{t}$	0.8	10^7	10^4 Tevatron-II
$b\bar{b}$ $p_T> 10\text{GeV}$	100K	2×10^{12}	
triggered with di-muon	10	10^8	10^8 Belle
SM Higgs (M=130GeV)	100 events/hour	5×10^5	
SUSY (M=1TeV)	10 events/hour	5×10^4	

the Higgs boson(s) and various fermions will give insights to the origin of mass. Discovery and the detail studies on the various properties of Higgs boson(s) are the primary subject at LHC, and the most urgent issue of the modern particle physics.

In the Standard model, one doublet of Higgs field is economically assumed, leading to the existence of one neutral scalar particle (H^0_{SM}). The Higgs boson mass is not theoretically predicted by the Standard model, but it's upper-limit is considered to be about 1 TeV, which is obtained from the unitary bound of is the W^+W^- scatter. Furthermore the Standard model Higgs is expected to be lighter than about 200 GeV (95%C.L.) with the precision measurements on the standard model processes at LEP[6]. The lower-limit on Higgs boson mass is 114 GeV obtained directly at LEP-II.

There are following four relevant production processes of the Higgs boson at LHC, and Fig. 2 shows the cross-section of each process as a function of the H^0_{SM} mass[7].

(a) $gg \rightarrow H^0_{SM}$: Gluon fusion process has the leading cross-section(20 pb for M_H=160 GeV), and H^0_{SM} is produced via the heavy quark loops[a]. Since there is no characteristic particle associate-produced with H^0_{SM}, it is difficult to find out Higgs boson decaying into hadron owing to the huge number of the QCD background. Only $H \rightarrow \gamma\gamma, ZZ(\rightarrow \ell\ell\ell\ell)$ and $W^+W^-(\rightarrow \ell\nu\ell\nu)$ decay modes are promising.

(b) $qq \rightarrow qq H^0_{SM}$: Vector Boson Fusion process has also large cross-section in the wide mass range as shown in Fig. 2. Since W and Z boson, which are exchanged in t-channel, are heavy, the out-going quarks have larger transverse momenta, p_T, than the QCD background processes. They will be observed in forward region(Forward jets)[8] with high p_T. Furthermore, there is no colour exchange between two out-going quarks, the Higgs boson will be observed in large rapidity gap. So it is promising channel for the various decay modes of H^0_{SM}.

(c) $q\bar{q} \rightarrow W/Z H^0_{SM}$: Higgs boson is associate-produced with a vector boson. It will be distinguished from the huge QCD backgrounds, when $W^\pm(Z^0)$ decays into leptons.

(d) $gg, q\bar{q} \rightarrow t\bar{t} H^0_{SM}$: H^0_{SM} is associate-produced with the top quark pair through large Yukawa coupling of top quark. Although production cross-section is relatively small (0.3 pb for 130 GeV) as shown in the figure, the huge QCD background events can be suppressed with tagging top pair. It is very promising channel for the light Higgs boson ($< 130 \sim$ 140 GeV). $gg, q\bar{q} \rightarrow b\bar{b} H$ process is also possible through the Yukawa coupling of bottom quark, but this channel is very difficult because of the QCD background ($gg \rightarrow b\bar{b}b\bar{b}$) for the standard Higgs boson. It becomes very important for the MSSM heavy Higgs bosons with a large value of $\tan \beta$, since the cross-section of $b\bar{b}H$ is enhanced by factor of $(\tan \beta)^2$.

Figure 3 shows the decay branching fraction of H^0_{SM} as a function of Higgs mass[7,9]. H^0_{SM} decays mainly into $b\bar{b}$ and $\tau^+\tau^-$ for the lighter case ($<$130 GeV). On the other hand, the decays into W^+W^- and ZZ have a large fraction for the heavier case ($>$140 GeV). Although the decay into $\gamma\gamma$ is suppressed due to one-loop process including heavy quarks, this decay mode has a sizable fraction for the case of (100–130 GeV). As mentioned in section 2.1, this decay mode is very important at LHC. Since mass of H^0_{SM} is expected to be within 114 – 200 GeV with the precision measurements on the standard model processes at LEP[6], all five decay modes ($b\bar{b}$, $\tau^+\tau^-$, $\gamma\gamma$, W^+W^- and ZZ) are important and should be covered.

2.1 $H^0_{SM} \rightarrow \gamma\gamma$

The branching fraction of this decay mode is small and there is a large background processes via $q\bar{q}, gg \rightarrow \gamma\gamma$. Also the bremsstrahlung process $qg \rightarrow \gamma q(\rightarrow \gamma q)$ contributes background events.

[a] The contribution of the top quark dominates, small contributions (about 5%) comes from the bottom quark.
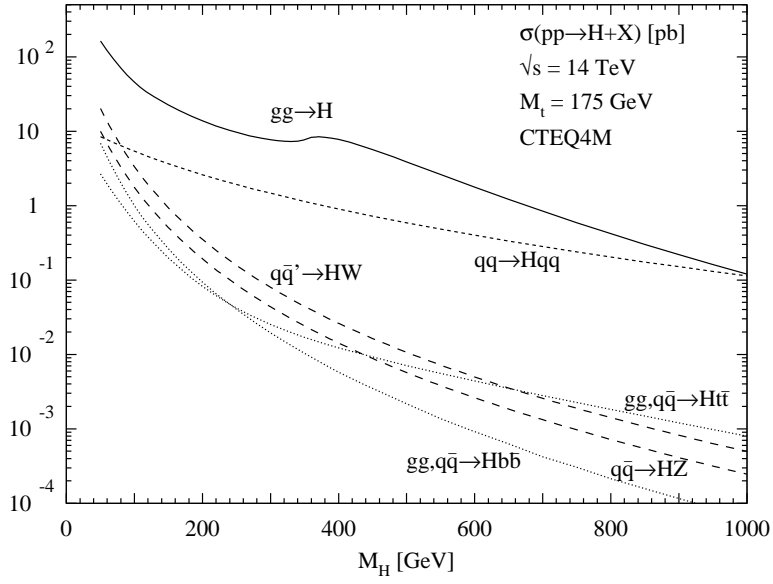
Figure 2: Production cross-section of H^0_{SM} as a function of the mass for the various processes (NLO calculation).
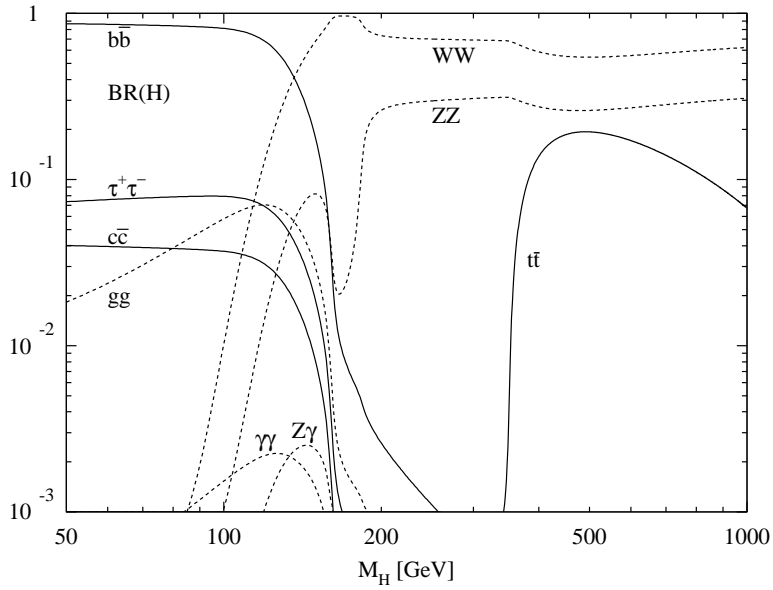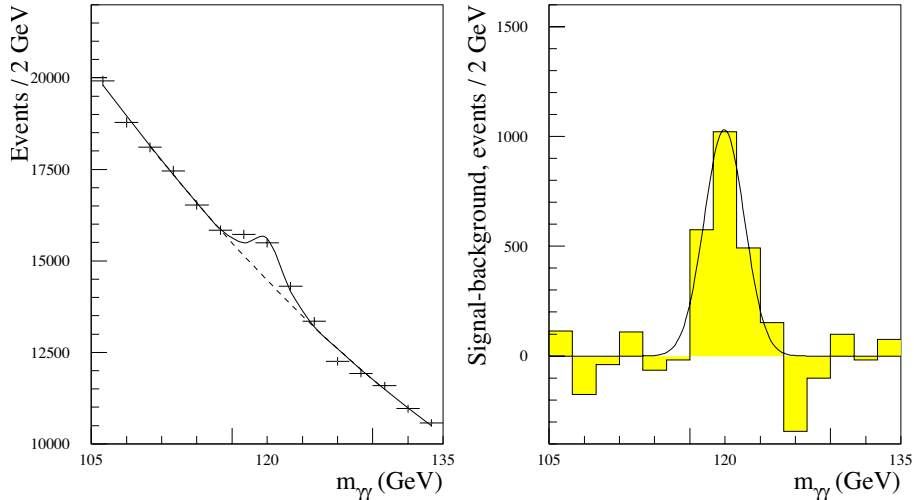

Figure 3: Decay branching fraction of H^0_{SM}.

Figure 4: The invariant mass distribution of $\gamma\gamma$ (L=100 fb^{-1} at ATLAS). M(H$^0_{SM}$)=120 GeV. Left figure shows signal plus background events, and right shows subtracted spectrum. In addition to $\gamma\gamma$ background, there are jet-γ and jet-jet background events.

But both ATLAS[4] and CMS[5] detectors have the excellent energy and position resolutions for photon. A mass resolution of H$^0_{SM} \to \gamma\gamma$ process is 1.1 GeV(ATLAS) and 0.6 GeV(CMS) at the low luminosity run. It becomes slightly worse to 1.3 GeV(ATLAS) and 0.7GeV(CMS) at the design luminosity due to the pile up effect[b], but it is still good enough to distinguish the signal from the background events as shown in Fig. 4. Sharp peak appears at Higgs boson mass over smooth distribution of the background events.

Detection efficiency of two isolate γ's is expected to be higher at ATLAS because of the large acceptance and better performance on the identify γ-conversion inside the inner detector. Both detectors have the similar sensitivity to find out H$^0_{SM} \to \gamma\gamma$ process[10]. This channel is promising for the light Higgs boson, whose mass is within 90 and 130 GeV.

2.2 $gg \to$ H$^0_{SM}$ ($\to ZZ \to \ell^+\ell^-\ell^+\ell^-$)

Dominant decay modes of the heavy H$^0_{SM}$ become into ZZ and W^+W^- as shown in Fig. 3. Four-lepton channel(H$^0_{SM} \to ZZ \to \ell^+\ell^-\ell^+\ell^-$) is very clean and the gold-plated in these bosonic decays. Although the branching fraction of $ZZ \to \ell^+\ell^-\ell^+\ell^-$ is small, a sharp mass peak is expected as shown in Fig. 5. Mass resolutions of four lepton system are 1.6 and 2.2 GeV for M(H^0_{SM})=130 and 180 GeV, respectively[11]. The $\ell^+\ell^-\ell^+\ell^-$ channel has a good performance in the wide mass range from 130 to 1000 GeV, except for 170 GeV. When Higgs mass is 170 GeV, the branching fraction of H$^0_{SM} \to W^+W^-$ is almost 100%, and this case is well covered by the other analysis of H$^0_{SM} \to W^+W^-$.

2.3 $qq \to qq$ H$^0_{SM}$: Vector Boson Fusion

The out-going quarks are observed in the forward regions, and have large p_T of about half of $W^\pm$ and Z^0 masses. Tagging these forward jets suppress the background events. H$^0_{SM} \to \tau^+\tau^-$ provides high p_T $\ell^\pm$ in the case of a leptonic τ-decay, and it can be clearly used as trigger. Momenta carried by ν's emitted from τ decays can be estimated approximately using the $\not{E}_T$

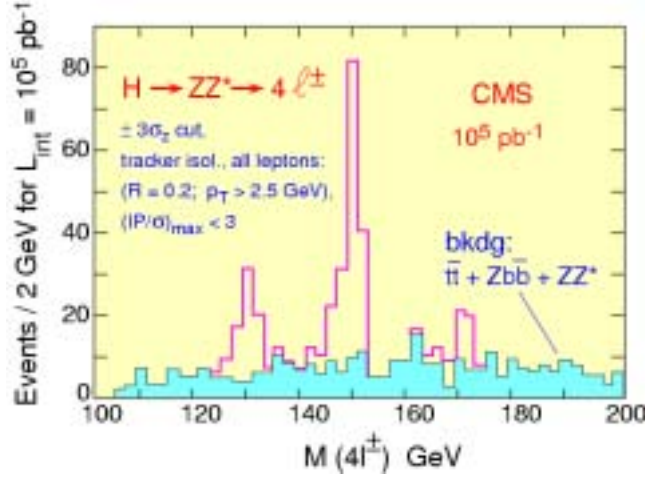---

[b]23 minimal bias events are piled up at the design luminosity.

Figure 5: The invariant mass distribution of $\ell^+\ell^-\ell^+\ell^-$ (L=100 fb^{-1} at CMS). Open histogram shows the signal with M(H$^0_{SM}$)=130,150 and 170 GeV, and clear peak is observed. On the other hand, hatched histogram shows the distribution of the ZZ background events, and it is flat distribution.

information [c], and Higgs mass can be reconstructed [12]. Typical mass resolutions are about 10 − 13 % depending on the Higgs mass, and signal can be clearly separated from the background events as shown in Fig. 6. Dominant background process is Drell-Yan with two high $p_T$jets, and the invariant mass distribution of the reconstructed tau pair makes peak at Z^0 mass. Careful investigations of this channel have been performed, and we can find this channel is the most promising to discover Higgs boson whose mass is smaller than 130 GeV.

H$^0_{SM} \to$ W$^+$W$^- \to \ell\nu\ell\nu$ channel also provides a good sensitivity as shown in Fig. 7. Although Higgs mass can not be reconstructed in this Jannel, large excess will be observed [12] in the transverse mass distribution of two leptons and $\not{E}_T$. This channel covers the region of $m_{H^0_{SM}} > 130\ GeV$, since the branching fraction of H$^0_{SM} \to$ W$^+$W$^-$ increases.

2.4 Overall discovery potential of H$^0_{SM}$

Promising channels to discover Higgs and study of its properties are summarized in table 2. We have various channels to discover, and also we can measure mass and couplings of Higgs boson. Discovery potential of H$^0_{SM}$ are shown in Fig. 8 as a function of Higgs mass with an integrated luminosity of 30 fb^{-1}. Vector Boson Fusion process in which H$^0_{SM} \to \tau^+\tau^-$ and H$^0_{SM} \to$ W$^+$W$^-$ provide excellent sensitivity in the mass region between 110–130 GeV and 130–180 GeV, respectively. A significance combined with 6 promising channels [12] is larger than 8 σ, i.e. we can perform 5 σ discovery of Higgs boson (M=114-200 GeV) within the first year run(10 fb^{-1}). For heavy case, ($\geq$ 200 GeV), decay to Z$Z(\to \ell^+\ell^-\ell^+\ell^-)$ has an excellent performance much higher than 10σ. **A critical test on the Higgs mechanism can be performed within the first year at LHC.**

We have also enormous potential to discover MSSM Higgs bosons as the same as H$^0_{SM}$. The lightest CP-even Higgs boson is expected to be very similar to H$^0_{SM}$, and there is no difficulties to discover as mentioned above. Also the other Higgs bosons (Heavy CP-even state, CP-odd, and charged Higgs) can be discovered directly, when $\tan\beta$ is larger than 5 and M_A is smaller than 1 TeV [4].

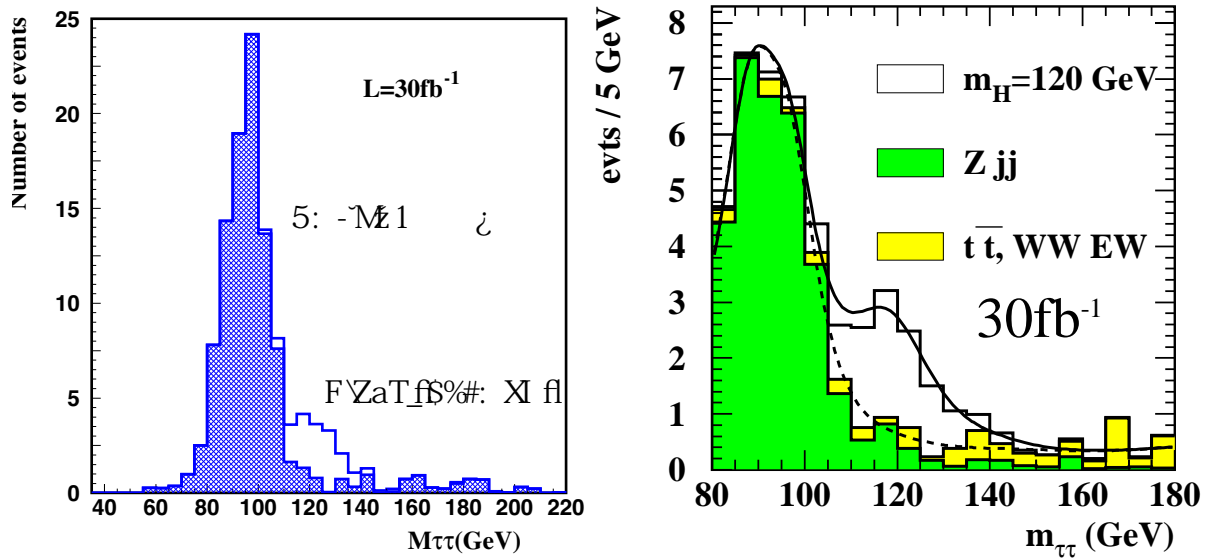[c]ν is assumed to emit in the same direction of the observed particles.

Figure 6: The invariant mass distributions of the reconstructed $\tau\tau$ (L=30 fb^{-1} at ATLAS) for M(H$^0_{SM}$)=120 GeV. Left figure shows the semi-leptonic decay of tau pair and right shows case in which the both τ decay leptonically. In both figures open histogram show the distribution of signal and the hatched histogram show the distribution of the background processes, Drell-Yan process is dominant.
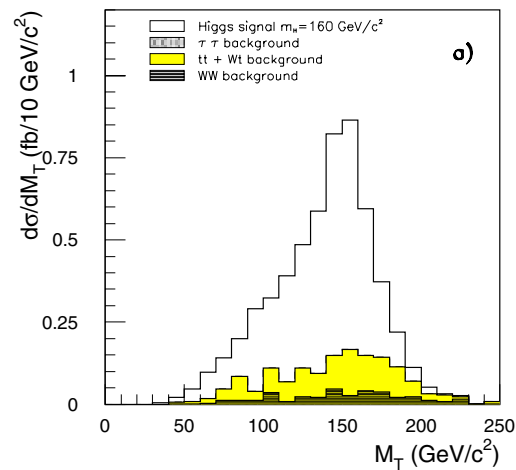

Figure 7: The transverse mass distribution of the $\ell\ell$ and $E\!\!\!/_T$ for M(H$^0_{SM}$)=170 GeV. Open and hatched histogram show the distribution of signal and and the background processes, respectively.

Table 2: Promising channels of Higgs study are summarized.

| Production process	Decay process	mass region (GeV)	Discovery channel or Which constant can be measured?
Gluon Fusion	$H \to \gamma\gamma$	110–140	Mass measurement
	$H \to ZZ \to \ell^+\ell^-\ell^+\ell^-$	140–1000	Discovery, mass, spin, g_{HZZ}
	$H \to W^+W^-$	130–170	Discovery
Vector Boson Fusion	$H \to \tau^+\tau^-$	110–140	Discovery, mass, g_{HWW}, y_τ
	$H \to W^+W^-$	130–200	Discovery, g_{HWW}
	$H \to \gamma\gamma$	110–140	Discovery? (still under way)
	$H \to b\bar{b}$	110–140	y_b ? (still under way)
ttH	$H \to b\bar{b}$	110–130	
	$H \to \tau^+\tau^-$	110–130	y_t
	$H \to W^+W^-$	130–180	
WH	$H \to W^+W^-$	140–170	Discovery, g_{HWW}
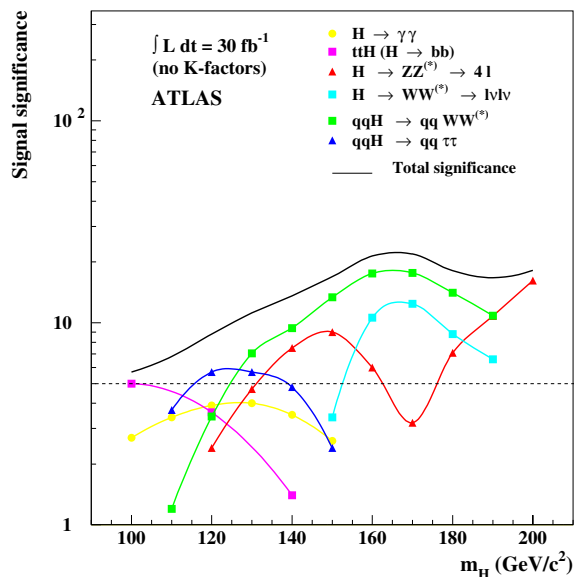
Figure 8: H^0_{SM} discovery potential with the integrated luminosity of 30 fb^{-1}. Horizontal axis is a mass of Higgs boson, and vertical axis is significance of Higgs signal. Horizontal dotted line shows 5σ. Only six channels are combined.
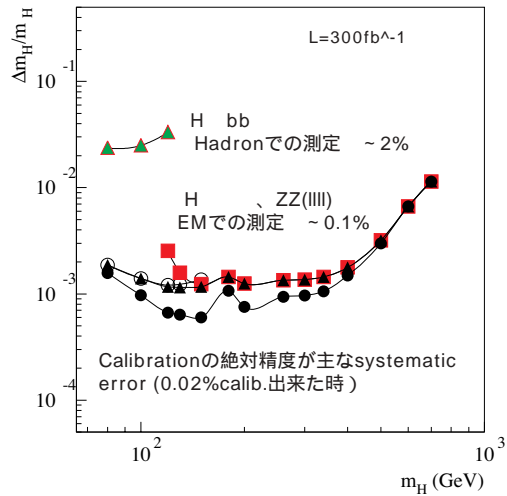
Figure 9: Relative precision on the measured Higgs boson mass as function of Higgs mass with an integrated luminosity is 300 fb^{-1}. The Black triangle and circles correspond to combined all channels with an assumption of uncertainty of 0.1% and 0.02%, respectively, on the absolute energy scale of EM counters.
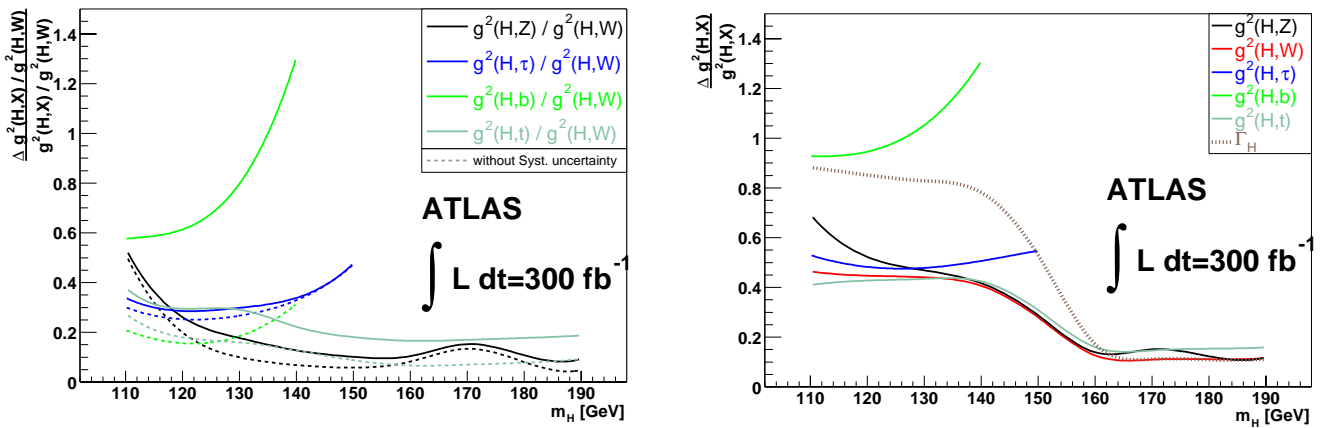

Figure 10: Precision on the measured coupling constant (square of constants) of Higgs boson mass as function of Higgs mass with an integrated luminosity is 300 fb^{-1}. Left figure shows accuracies of ratio normalized by g_{HWW}, and the right shows the accuracies of absolute values of coupling.

2.5 Measurement of mass and couplings of Higgs boson(s)

Measurements on the properties of the discovered Higgs boson(s) give furthermore insights to the Electroweak symmetry-braking mechanism and to the origin of masses. They are very important works and they maybe open a window of new epoch.

Figure 9 shows the precision on the measured mass of Higgs boson. The standard model Higgs boson is assumed on this study. Higgs mass can be measured with an accuracy of less than 0.2%, if the mass is smaller than 500 GeV. Main source of uncertainties is the accuracy of absolute calibration of energy scale in the Li.Ar calorimeter. When the Higgs boson is heavier than 500 GeV, the resonance of Higgs boson becomes too broad to determine the peak position, and the precision becomes worse.

Measurements of the couplings between Higgs boson and fermions/Gauge bosons will give the direct informations of origin of "Mass", and it will give the first evidence of Yukawa couplings. Accuracies of the measured ratio of the coupling are expected to be about 5–10, 10–15, 10–15 and 30–40% for g_{HZZ}/g_{HWW}, y_τ/g_{HWW}, y_t/g_{HWW} and y_b/g_{HWW}, respectively, as shown in Fig. 10(a). The absolute values of coupling constants (y_τ, y_t, g_{HWW} and g_{HZZ}) can be measured with an accuracy of about 20%, expect for y_b.

3 SUSY physics

Supersymmetric (SUSY) standard models [13] are most promising extensions of the standard model, because the SUSY can naturally deal with the problem of the quadratic Higgs mass divergence. Furthermore, the SUSY models provides a natural candidate for cold dark matter [14], and they have given a hint of the Grand Unification of gauge couplings around 2×10^{16} GeV. In these theories, each elementary particle has a superpartner whose spin differs by 1/2 from that of the particle. Discovery of these SUSY particles should open a window of new epoch, and is one of the important purpose of the LHC project.

There are, in general, more than 100 free parameters to describe SUSY soft breaking [13], following two SUSY models are predictable and promising.

- SuperGravity Model [15] assumes that gravity is responsible for the mediation of the SUSY breaking and provides a natural candidate for cold dark matter [14].

- Gauge-Mediated Model [16] assumes that standard model gauge interactions are responsible for the mediation. It naturally solves the FCNC problem.

Many studies have been performed on these two models and also the other models. Performance based on the SuperGravity model are summarized in this note.

3.1 Introduction of Minimal SuperGravity Model

3.1.1 General introduction

Minimal Super-Gravity Model (mSUGRA) [15] is a special case of the Minimal Supersymmetric Model (MSSM). In this model, the SUSY soft breaking terms are assumed to be communicated from the SUSY breaking sector by gravity. Furthermore, these SUSY soft breaking terms are universal at the GUT scale. There are only five parameters after imposing GUTs conditions;

- m_0: Universal mass of all scalar particles at GUT scale.

- $m_{1/2}$: Universal mass of all gauginos at GUT scale.

- A_0: Common trilinear coupling at GUT scale.

- $\tan \beta (\equiv v_2/v_1)$: Ratio of VEV of two Higgs fields at the Electroweak scale.

- $\text{sign}\mu$: ± 1, Sign of Higgsino mass term.

Masses of gluino, $\tilde{g}$ and gauginos are mainly determined by $m_{1/2}$. $\tilde{g}$ becomes heavy due to large radiative corrections, and its mass is approximately 2.6 $m_{1/2}$. Higgsino mass ($|\mu|$) becomes larger than gaugino mass at the EW scale, except for the case of $m_0 \gg m_{1/2}$. Then the lighter states of neutralino, $\tilde{\chi}_1^0$ and $\tilde{\chi}_2^0$, become almost pure gaugino states ($\tilde{\chi}_1^0 \sim \tilde{B}^0$, $\tilde{\chi}_2^0 \sim \tilde{W}^0$), and lighter state of chargino, $\tilde{\chi}_1^\pm$, is also gaugino-like ($\tilde{\chi}_1^\pm \sim \tilde{W}^\pm$). Scalar lepton masses are determined mainly by m_0 and weakly by $m_{1/2}$. On the other hand, scalar quark masses depend on both m_0 and $m_{1/2}$.

- $m(\tilde{g}) \sim 2.6 \ m_{1/2}$.

- $m(\tilde{\chi}_1^0) \sim 0.4 \ m_{1/2}$.

- $m(\tilde{\chi}_2^0) \sim m(\tilde{\chi}_1^\pm) \sim 0.8 \ m_{1/2}$.

- $m(\tilde{\ell}_R^\pm) \sim \sqrt{m_0^2 + 0.15 m_{1/2}^2}$

Table 3: Summary of decay modes of $\tilde{\chi}_2^0$

decay mode	condition and remarks
$\tilde{\chi}_2^0 \to \tilde{\ell}^{\pm}\ell$	$m_{\tilde{\ell}^{\pm}} < m_{\tilde{\chi}_2^0}$
$\quad \to \ell\tilde{\chi}_1^0$	(Remarks) $\tilde{\chi}_2^0 \to \tilde{\tau}\tau$ for $(\tan\beta \gg 1)$
$\tilde{\chi}_2^0 \to h\tilde{\chi}_1^0$	$m_{\tilde{\chi}_2^0} - m_{\tilde{\chi}_1^0} > m_h$
$\tilde{\chi}_2^0 \to Z^0\tilde{\chi}_1^0$	$m_h > m_{\tilde{\chi}_2^0} - m_{\tilde{\chi}_1^0} > m_{Z^0}$
$\tilde{\chi}_2^0 \to f\bar{f}\tilde{\chi}_1^0$	3-body decay, other cases

- $m(\tilde{\ell}_{\rm L}^{\pm}) \sim \sqrt{m_0^2 + 0.5m_{1/2}^2}$

- $m(\tilde{q}_{{\rm L},R}) \sim \sqrt{m_0^2 + 6m_{1/2}^2}$

Masses of 3rd generation scalar fermions ($\tilde{t}_1$, $\tilde{b}_1$, and $\tilde{\tau}_1$) depend also on A and $\tan\beta$ [18], and they are generally lighter than first and second generations because of the following two reasons. Firstly, one loop radiative corrections to these masses are always negative, and corrections are proportional to Yukawa coupling. Secondly, the supersymmetric partners of the right-handed and left-handed states mix, and the resultant two mass eigenstates have a large mass splitting. This mixing contribution depends on both A_0 and $\tan\beta$.

3.1.2 Production and Decay processes

Dominant SUSY production processes at LHC are $\tilde{g}\tilde{g}$, $\tilde{g}\tilde{q}$ and $\tilde{q}\tilde{q}$ through the strong interaction. These production cross-sections, σ, do not strongly depend on the SUSY parameters except for masses of $\tilde{g}$ and $\tilde{q}$ [19]. When these masses are 500 GeV, $\tilde{g}\tilde{g}$ is main production process, and total $\sigma(\tilde{g}\tilde{g}$, $\tilde{g}\tilde{q}$ and $\tilde{q}\tilde{q})$ is 100 pb. σ becomes 3 pb for $m_{\tilde{q}}=m_{\tilde{g}}=1$TeV. Even when these masses are 2 TeV, sizable production cross-section of about 20 fb is expected. $\tilde{u}\tilde{u}$ and $\tilde{u}\tilde{d}$ are main production processes for such a heavy case, since u and d quarks are valence quarks. K-factors are about 1.4 [20] for the $\tilde{g}\tilde{g}$, $\tilde{g}\tilde{q}$ and $\tilde{q}\tilde{q}$ production processes (virtual effect), and it is modest value as same as the case of Higgs boson. But all studies presented in this document are based on Leading Order Monte Calro simulations [21,22].

Decay modes of $\tilde{g}$ and $\tilde{q}$ are controlled by the mass-relation between each other, and are summarized in table above. If kinematically possible, they decay into 2-body through the strong interaction. Otherwise, they decay into a Electroweak gaugino plus quark(s). Bino/Wino-eigenstates presented in this table become simply mass-eigenstate, ($\tilde{B}^0 \sim \tilde{\chi}_1^0$, $\tilde{W}^0 \sim \tilde{\chi}_2^0$, and $\tilde{W}^{\pm} \sim \tilde{\chi}_1^{\pm}$), when m_0 is not too larger than $m_{1/2}$. In this case, Higgsino mass ($|\mu|$) becomes larger than gaugino mass at the EW scale, then Higgsino component decouples from lighter mass-eigenstates as already mentioned. Decay modes of third generation squarks ($\tilde{t}_1$ and $\tilde{b}_1$) are more complicated, since they have enough coupling to Higgsino due to non-negligible Yukawa couplings.

There are four leading decay modes of $\tilde{\chi}_2^0$ depending on mass spectrum. These are summarized in table 3 with the conditions of mass spectrum. When the scalar lepton, $\tilde{\ell}^{\pm}$, is lighter than $\tilde{\chi}_2^0$, 2-body decay chain, $\tilde{\chi}_2^0 \to \ell\tilde{\ell}^{\pm}(\to \ell\tilde{\chi}_1^0)$ becomes dominant decay mode. Branching fraction of $\tilde{\chi}_2^0 \to \tau\tilde{\tau}_1$ is significant large in the case of $\tan\beta \gg 1$. $\tilde{\chi}_2^0 \to h\tilde{\chi}_1^0$ is dominant mode, if the mass difference between $\tilde{\chi}_2^0$ and $\tilde{\chi}_1^0$ is larger than Higgs boson mass. When the mass difference is smaller than m_{Z^0}, three body decay is main decay process. $\tilde{\chi}_1^{\pm}$ has three leading decay modes, $\tilde{\chi}_1^{\pm} \to \tilde{\ell}^{\pm}\nu$, $W^{\pm}\tilde{\chi}_1^0$ and $f\bar{f}'\tilde{\chi}_1^0$ as the similar manner to $\tilde{\chi}_2^0$.

$\tilde{g}, \tilde{q}$ の decay table

	$m(\tilde{g}) < m(\tilde{q})$	$m(\tilde{g}) \approx m(\tilde{q})$	$m(\tilde{g}) > m(\tilde{q})$
$\tilde{g}$	$\tilde{g} \to \begin{cases} q\bar{q}\tilde{B}^0 \, (\approx 1) \\ q\bar{q}\tilde{W}^0 \, (\approx 2) \\ q\bar{q}\tilde{W}^{\pm} \, (\approx 4) \end{cases}$	$\tilde{g} \to \begin{cases} t\tilde{t}_1 \\ b\tilde{b}_1 \end{cases}$	$\tilde{g} \to q\tilde{q}$
$\tilde{q}_L$	$\tilde{q}_L \to q\tilde{g}$	$\tilde{q}_L \to \begin{cases} q\tilde{W}^0 \, (\approx 1) \\ q\tilde{W}^{\pm} \, (\approx 2) \end{cases}$	
$\tilde{q}_R$	$\tilde{q}_R \to q\tilde{g}$	$\tilde{q}_R \to q\tilde{B}^0$	

Figure 11:

3.2 Event topologies of mSUGRA events and discovery potential

$\tilde{g}$ and/or $\tilde{q}$ are copiously produced at the LHC with $p_T \sim$ M. High p_T jets are emitted from the decays of $\tilde{g}$ and $\tilde{q}$ as shown in table ??. Each event contains two $\tilde{\chi}_1^0$'s in the final state. If R-parity [17] is conserved, $\tilde{\chi}_1^0$ is stable, and it is neutral and weakly interacting and escape from the detection. Then missing transverse energy, $\not{E}_T$, carried away by two $\tilde{\chi}_1^0$'s plus multiple high p_T jets is the leading experimental signature of SUSY. Also the other activities of additional jets, leptons and $b\bar{b}$ are possible, coming from the decays of $\tilde{\chi}_2^0$ and $\tilde{\chi}_1^{\pm}$. These additional informations are important to confirm SUSY signals, and to investigate its properties.

The following four standard model processes can potentially have $\not{E}_T$ event topology with jets.

- $W^{\pm}$ + jets, $W^{\pm} \to \ell\nu$

- Z^0 + jets, $Z^0 \to \nu\bar{\nu}, \tau^+\tau^-$

- $t\bar{t}$

- QCD jets with mismeasurement

SUSY signals should be observed as an excess of these standard model processes. Large significance can be obtained for SUSY signals after large $\not{E}_T$ and p_T are respectively required on event and jets. $\not{E}_T + \sum_{jets} p_T$ is a good variable [11] to see an excess coming from the SUSY signals as shown in Fig. 12. The distribution of $\not{E}_T + \sum_{jets} p_T$ has steep slop for the standard model background processes as shown in this figure. On the other hand, the distribution for the SUSY signals has a peak at large value, and long tail contribute to the higher side. The shape quite differs from that of the background processes. This peak position has a good sensitivity to $min(m(\tilde{g}), m(\tilde{q}))$, and it can be determined with accuracy of 15% [23] using this variable. It will be discussed later. Independent excesses are also expected in the other topologies, for example, $\not{E}_T$ + jets + isolated lepton(s). This isolated lepton will be emitted from $\tilde{\chi}_2^0$ and $\tilde{\chi}_1^{\pm}$.
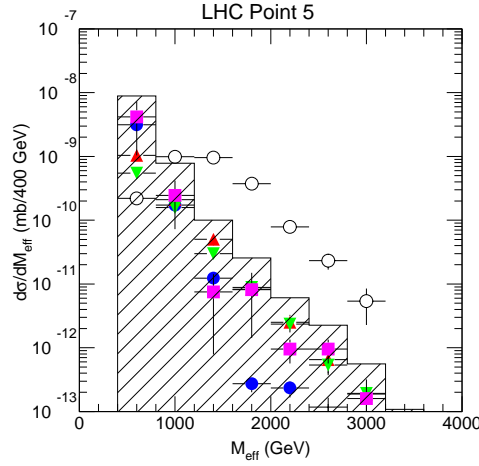
Figure 12: $\not{E}_T + \sum_{jets} p_T$ distributions: (open circles) for SUSY signals at LHC point 5, and (histogram) for sum of all standard model backgrounds. It includes the followings: $t\bar{t}$(black circles), $W^{\pm}$ + jets(triangles), Z^0 + jets(downward-triangles), and QCD(squares).

Figure 13 shows 5σ-discovery potential in m_0-$m_{1/2}$ plane for $\tan \beta = 35$ using the $\not{E}_T$ plus jets channel with various integrated luminosities. Mass contours for $\tilde{g}$ and $\tilde{q}$ are also super-imposed. As shown in this figure, $\tilde{g}$ and $\tilde{q}$ can be discovered close to $M \sim 1.5$ TeV with a luminosity of 1 fb^{-1}, which is corresponding to just one month run with $10^{33} cm^{-2} s^{-1}$. The interesting region for relic density of the dark matter is almost covered with just 1 fb^{-1}. We can discover $\tilde{g}$ and $\tilde{q}$, whose masses less than about 2.0 TeV within one year, corresponding a luminosity of 10 fb^{-1}. $\tilde{g}$ and $\tilde{q}$, whose masses are about 2.5 TeV, can be discovered finally with a luminosity of 300 fb^{-1}. This luminosity is corresponding to three years run with design luminosity of $10^{34} cm^{-2} s^{-1}$. **Both ATLAS [11] and CMS [24] collaborations have an excellent potential to discover SUSY, and they will cover interesting parameter region predicted by naturalness [13] and relic density of dark matter [13,14].**

3.3   Measurements of masses of SUSY particles

Since two undetected LSP's exist in each event, there are six unknown momentum components in addition to the $\tilde{\chi}_1^0$ mass. So no mass peak is expected in general. However it is possible to use kinematic end points of various distributions as follows [11,24].

- (1) Select specific decay chain exclusively. For example,

$$
\begin{aligned}
\tilde{g} &\rightarrow \tilde{q}_L q \\
&\rightarrow \tilde{\chi}_2^0 q \\
&\quad\rightarrow \tilde{\ell}^{\pm}\ell \\
&\quad\quad\rightarrow \tilde{\chi}_1^0 \ell
\end{aligned}
$$

- (2) Make various distributions of invariant masses and p_T.

- (3) kinematic constraints are obtained from edges and end points of these distributions. These edges and end points are combinations of the masses, and these are just determined by the kinematics and not depend on the other SUSY parameters.
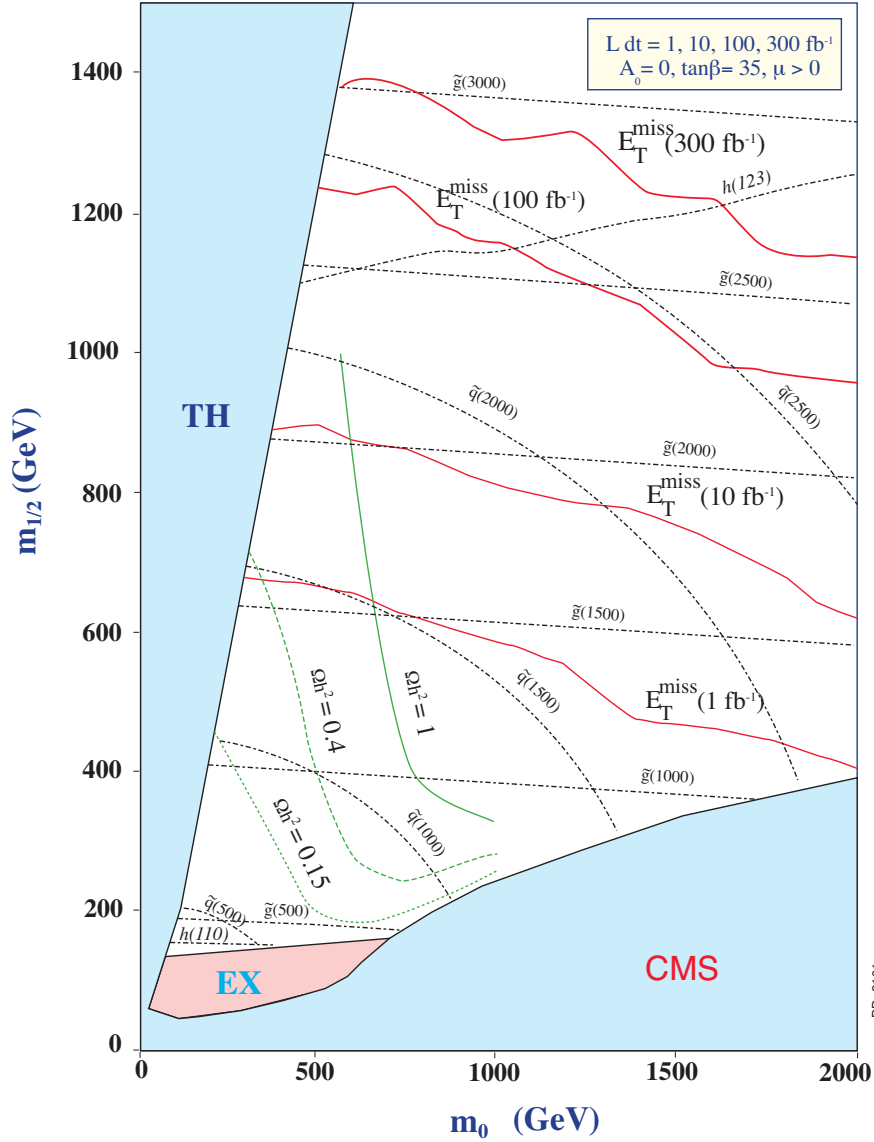
Figure 13: 5σ-discovery region in m_0-$m_{1/2}$ plane for $\tan\beta = 35$ using the $\not{E}_T$ plus jets channel. Mass contours for $\tilde{g}$ and $\tilde{q}$ are also superimposed. Ωh^2 shows relic density of the dark matters. In the gray region, $\tilde{\ell}^\pm$ becomes the LSP, or no Electroweak symmetry breaking occurs.
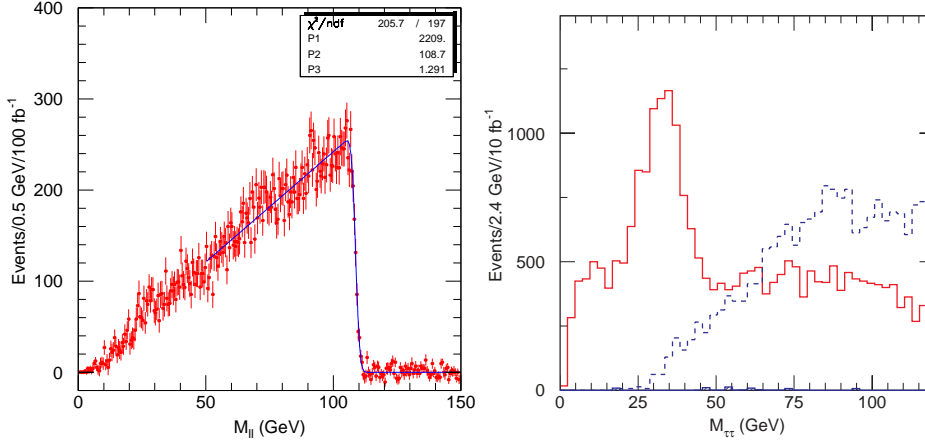
Figure 14: (a) Invariant mass distribution for the di-lepton system ($e^+ e^-$ and $\mu^+ \mu^-$) (at LHC point 5). Flavour subtraction, $e^+ e^- + \mu^+ \mu^- - e^+ \mu^- - e^- \mu^+$, has been performed. (b) Invariant mass distribution for identified τ-pair system(at LHC point 6). Solid line shows distribution for the correct τ-pair, and dotted line shows the contribution from fake τ.

If there are at least three 2-body decays like this example, full reconstruction of masses is possible model-independently. It is important remark. When we can not find out such three 2-body decays, number of obtained constraint is less than number of unknown masses. Some assumption is necessary to determine mass spectrum of SUSY. SUSY events become background itself for detailed study, since there are many cascade decay patterns in $\tilde{q}$ and $\tilde{g}$.

3.3.1 Kinematic edges for $\tilde{\chi}_2^0$ decay:

$\tilde{\chi}_2^0 \rightarrow \ell \tilde{\ell}^\pm (\rightarrow \ell + \tilde{\chi}_1^0)$ is the dominant decay mode, when $\tilde{\ell}^\pm$ is lighter than $\tilde{\chi}_2^0$. This is corresponding to the parameter space of $m_0 < \sim 0.8 m_{1/2}$.

The same flavour opposite charge di-lepton($\ell = e, \mu$) is the characteristic signal. Figure 14(a) shows invariant mass distribution of the di-lepton system. Flavour subtraction, $e^+ e^- + \mu^+ \mu^- - e^+ \mu^- - e^- \mu^+$, has been performed to suppress flat distribution comes from chargino and $t\bar{t}$ decays. Sharp edge ($M_{\ell\ell}^{max}$) is observed, and it is related to

$$M_{\ell\ell}^{max} = m(\tilde{\chi}_2^0) \sqrt{1 - (m(\tilde{\ell}^\pm)/m(\tilde{\chi}_2^0))^2} \sqrt{1 - (m(\tilde{\chi}_1^0)/m(\tilde{\ell}^\pm))^2}. \tag{1}$$

This can be determined very precisely. Statistical error is 0.1% with L=100 fb^{-1} for this case (it strongly depends on $\sigma \times Br$), and systematic error is less than 0.1%, mainly comes from uncertainty of the energy scale calibration. Figure 15 shows the parameter region in which $M_{\ell\ell}^{max}$ can be determined. $M_{\ell\ell}^{max}$ originated from 2-body decay ($\tilde{\chi}_2^0 \rightarrow \tilde{\ell}_L \ell$ and $\tilde{\chi}_2^0 \rightarrow \tilde{\ell}_R \ell$) can be observed in a wide region as presented in this figure.

Furthermore, an asymmetry of p_T of two leptons,

$$A_{\ell\ell} = \frac{p_T^{max} - p_T^{min}}{p_T^{max} + p_T^{min}}, \tag{2}$$

has also information on $\tilde{\ell}^\pm$ mass [25]. As $\tilde{\ell}^\pm$ mass is heavier, asymmetry, $A_{\ell\ell}$, becomes larger. Above two kinematic constraints are obtained from the di-lepton system.

When $\tan \beta$ is much larger than 1, $\tilde{\tau}_1$ becomes much lighter than $\tilde{e}_R$ and $\tilde{\mu}_R$, and $\tilde{\chi}_2^0 \rightarrow \tilde{\tau}_1 \tau$ can become dominant decay mode [26]. Hadronic decay mode of τ is used for a τ-identification. The followings are essence of the τ-identification, and the selection efficiency is about 40%:
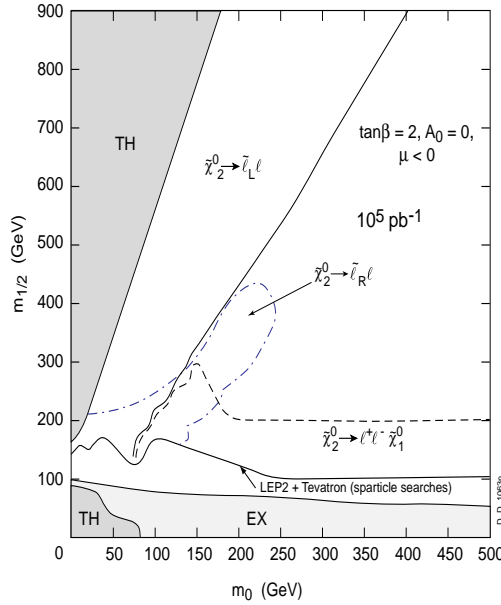
Figure 15: Parameter region for observing the edge of $M_{\ell^+\ell^-}$ due to $\tilde{\chi}_2^0 \to \tilde{\ell}_L \ell$ (solid), $\tilde{\chi}_2^0 \to \tilde{\ell}_R \ell$ (dashed-dotted) and $\tilde{\chi}_2^0 \to \ell^+ \ell^- \tilde{\chi}_1^0$ (dashed).

- 1-3 prong is selected.

- Energy deposited in calorimeter and these tracks are well concentrated in narrow cone(R=0.2).

- This activity are well isolated from jet activities.

Figure 14(b) shows $M_{\tau\tau}$ distribution, which is visible invariant mass of $\tau\tau$ system times $1/0.66$. This factor is mean value to correct the energy carried by neutrinos. Flat contribution in this distribution comes from $\tilde{\chi}_1^\pm \to \tilde{\tau}\nu$. Kinematic edge can be also observed even in the τ case, and this can be determined with accuracy of about 5%. This edge is related to various masses in eq.(1).

$\tilde{\chi}_2^0 \to h\tilde{\chi}_1^0$ becomes the dominant decay mode, when $\tilde{\ell}^\pm$ is heavier than $\tilde{\chi}_2^0$ and the mass difference between $\tilde{\chi}_2^0$ and $\tilde{\chi}_1^0$ is larger than m_h. It is corresponding to the parameter space of $0.4 \ m_{1/2} > m_h$. Fig. 16(a) shows the $M_{b\bar{b}}$ distribution, and a clear peak is observed at Higgs boson mass(h^0). This peak can been seen with more than 5σ-significance in a wide parameter region as shown in Fig. 16(b). Events in this peak can be used for reconstruction of decay chain including $\tilde{\chi}_2^0$ as mentioned later. Events with $\tilde{\chi}_2^0 \to Z^0 \tilde{\chi}_1^0$ also can been used in the same manner.

Figures 17 show invariant mass distributions of same flavour opposite charge di-lepton($\ell =$ e, μ) system for the 3-body decay of $\tilde{\chi}_2^0$. This decay mode becomes dominant, when the mass difference between $\tilde{\chi}_2^0$ and $\tilde{\chi}_1^0$ is smaller than M_Z. Sharp kinematic edges($M_{\ell\ell}^{max}$) are observed in both parameter points. Figure 15 shows the parameter region in which the $M_{\ell\ell}^{max}$ can be determined with L=100 fb^{-1}. $M_{\ell\ell}^{max}$ originated from 3-body decay can be observed in wide region. $M_{\ell\ell}^{max}$ is related to mass difference between $\tilde{\chi}_2^0$ and $\tilde{\chi}_1^0$, i.e.

$$M_{\ell\ell}^{max} = m(\tilde{\chi}_2^0) - m(\tilde{\chi}_1^0). \tag{3}$$

This kinematic edge can be determined very precisely as the same as 2-body decay case.

For $\ell^+\ell^-$ near the kinematic end point, momentum of $\tilde{\chi}_2^0$ in Lab-frame, $\vec{P}(\tilde{\chi}_2^0)$, can be directly reconstructed event by event, since $\ell^+\ell^-$ and $\tilde{\chi}_1^0$ almost stand still in $\tilde{\chi}_2^0$ rest-frame.

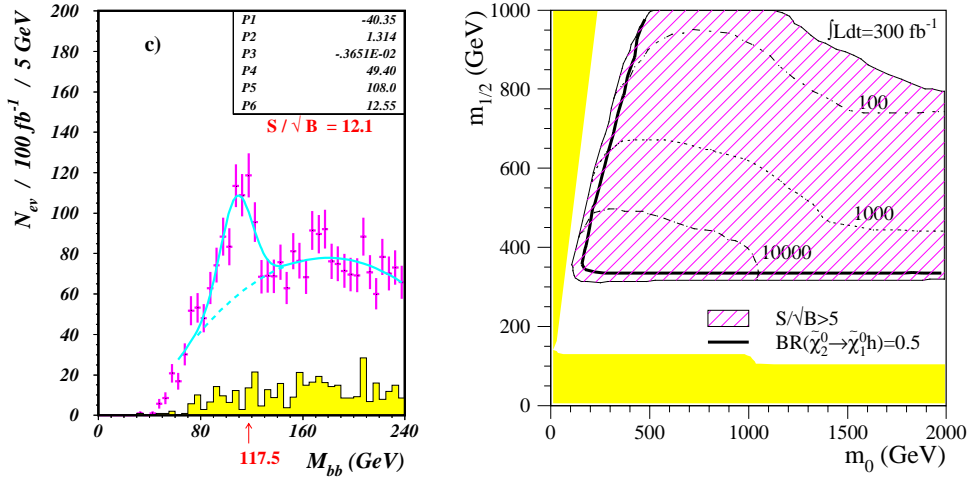$$\vec{P}(\tilde{\chi}_2^0) = (1 + m(\tilde{\chi}_1^0)/m(\ell^+\ell^-))\vec{P}(\ell\ell) \tag{4}$$

Figure 16: (a) Invariant mass distribution for $b\bar{b}$ system for $\tan\beta = 10$ ($m_0 = m_{1/2} = 500$ GeV and $\mu < 0$). Hatched histogram shows the background contribution from the standard model processes. (b) 5σ-visibility contour in m_0-$m_{1/2}$ plane for $\tan\beta = 10$ with luminosity of 300 fb^{-1}.
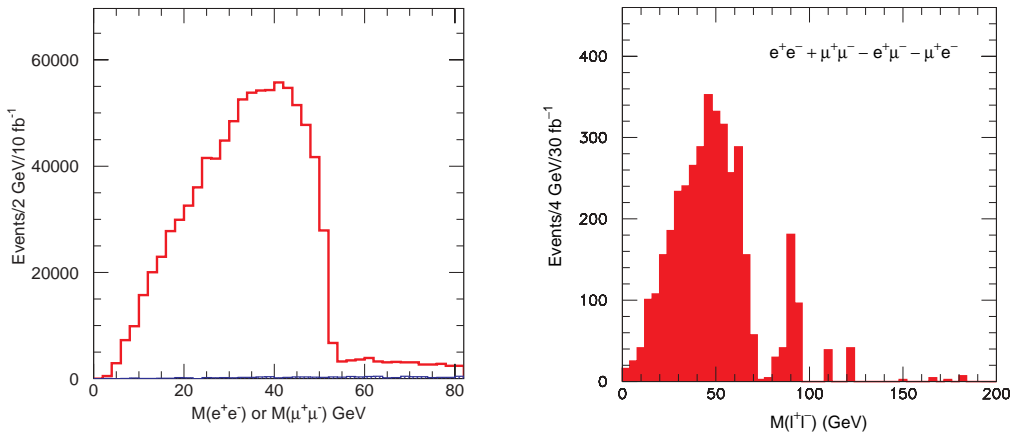

Figure 17: Invariant mass distributions for di-lepton system (e^+e^- and $\mu^+\mu^-$) Left histogram shows the case of small m_0 (at LHC point 3) and right shows large m_0 (at LHC point 4).

Four-momentum of $\tilde{\chi}_2^0$ can be reconstructed assuming relation between $m(\tilde{\chi}_1^0)$ and $m(\tilde{\chi}_2^0)$, since mass difference between $\tilde{\chi}_1^0$ and $\tilde{\chi}_2^0$ is already measured from the kinematic edge.

Sharp peak is also observed at M_Z in right side of Fig. 17. This is contribution from the heavier state of chargino($\tilde{\chi}_2^\pm$) and neutralino($\tilde{\chi}_4^0$). When m_0 is much larger than $m_{1/2}$, Higgsino mass ($|\mu|$) is relatively small comparing Wino mass (otherwise, the Electroweak symmetry breaking has problem), then the resultant mass eigenstates of chargino and neutralino become the mixed states of Higgsinos and Wino. In such a case, there is substantial branching fraction of $\tilde{g} \to \tilde{\chi}_2^\pm f\bar{f}$, and Z^0 are produced from $\tilde{\chi}_2^\pm$. Momentum of the reconstructed Z^0 carries an information about mass of the parent chargino, $\tilde{\chi}_2^\pm$. Since a mean value of p_T^Z, $< p_T^Z >$, is proportional to the $\tilde{\chi}_2^\pm$ mass, it can be determined by the fitted $< p_T^Z >$ with an accuracy of 3% including systematic errors.

3.3.2 Kinematic end points of jets plus $\tilde{\chi}_2^0$:

$\tilde{\chi}_2^0$ is emitted mainly from $\tilde{q}_L \to q\tilde{\chi}_2^0$ and $\tilde{g} \to q\bar{q}\tilde{\chi}_2^0$ processes as presented in table **??**. An information about mass of the parent particles, $\tilde{q}_L$ and $\tilde{g}$, can be obtained as follows.

$\tilde{q}_L \to \tilde{\chi}_2^0 q$
$\quad \to \tilde{\ell}^\pm \ell$
$\quad\quad \to \tilde{\chi}_1^0 \ell$ (2-body decay chain)
$\quad \to \ell\ell\tilde{\chi}_1^0$ (3-body decay)
$\quad \to h\tilde{\chi}_1^0$
$\quad\quad \to b\bar{b}$ (h decay)

are the leading decay chains of $\tilde{q}_L$. Figures 18 show invariant mass distributions of q$\ell\ell$- and qbb-systems. Although distributions are smeared by the limited energy resolution for hadron jets, these distributions have kinematic end points. Effects of the energy resolution and gluon emission from q should be taken into account to determine the end point. These kinematic end points are related to

$$\mathrm{M}_{\ell\ell q}^{max} = \frac{\sqrt{m(\tilde{q}_L)^2 - m(\tilde{\chi}_2^0)^2}\sqrt{m(\tilde{\chi}_2^0)^2 - m(\tilde{\chi}_1^0)^2}}{m(\tilde{\chi}_2^0)}$$

$$(\mathrm{M}_{hq}^{max})^2 = m(h)^2 + \frac{m(\tilde{q}_L)^2 - m(\tilde{\chi}_2^0)^2}{2m(\tilde{\chi}_2^0)^2}$$

$$\times \left(m(\tilde{\chi}_2^0)^2 + m(h)^2 - m(\tilde{\chi}_1^0)^2 + \sqrt{(m(\tilde{\chi}_2^0)^2 - m(h)^2 - m(\tilde{\chi}_1^0)^2)^2 - 4m(h)^2 m(\tilde{\chi}_1^0)^2} \right) \quad (5)$$

and can be determined with an accuracy of a few %.

For 3-body decay of $\tilde{\chi}_2^0$, four-momentum of $\tilde{\chi}_2^0$ can be directly reconstructed assuming the relation between $m(\tilde{\chi}_1^0)$ and $m(\tilde{\chi}_2^0)$ as already mentioned. An Invariant mass distribution of jet and reconstructed $\tilde{\chi}_2^0$ is shown in Fig. 19. A peak appears at $m(\tilde{q}_L)$ and this can be determined directly with an accuracy of 5% including systematic errors.

There are four unknown masses ($\tilde{q}_L$, $\tilde{\chi}_2^0$, $\tilde{\ell}^\pm$ and $\tilde{\chi}_1^0$) in the following 2-body decay chain:
$\tilde{q}_L \to \tilde{\chi}_2^0 q$
$\quad \to \tilde{\ell}^\pm \ell$
$\quad\quad \to \tilde{\chi}_1^0 \ell$,

which is dominant mode in the parameter space of $m_0 < 0.8m_{1/2}$. Figure 14(a), 18(b) and 20 show the invariant mass distributions of $\ell\ell$, $\ell\ell$+jet, and ℓ+jet. Three kinematic end points and one threshold of 4-body system ($\ell^+\ell^- q\tilde{\chi}_1^0$) are observed in these figures, and **all four**
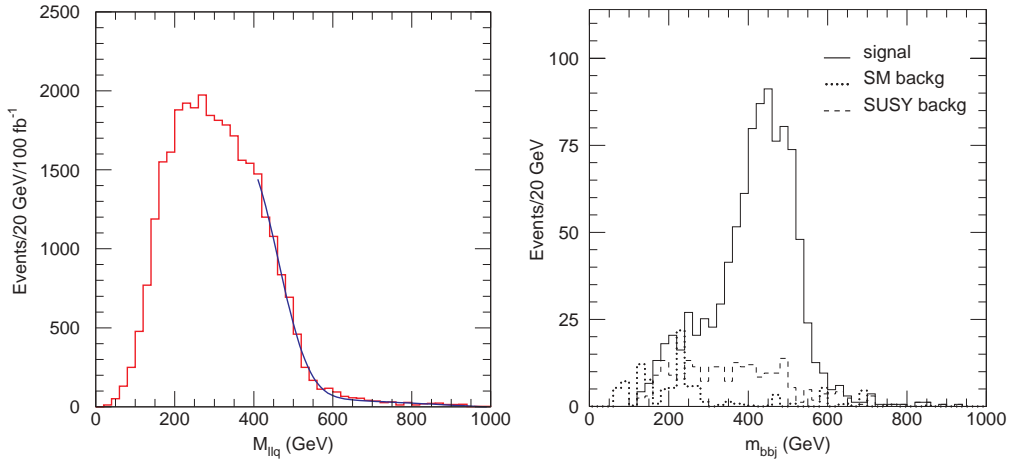
Figure 18: (a) Invariant mass distributions of qℓℓ (at LHC point 5). (b) Invariant mass distributions of qbb (at LHC point 1).
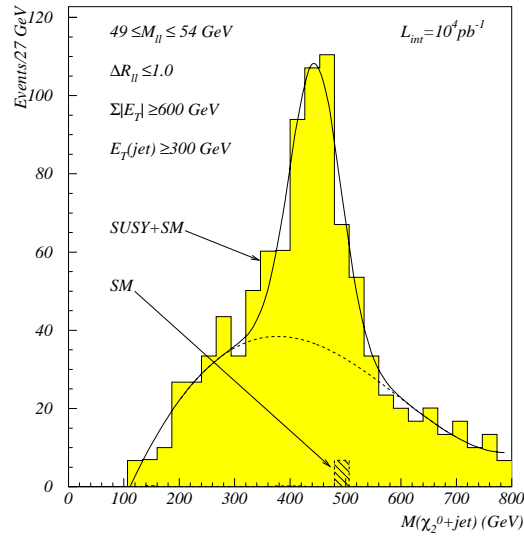

Figure 19: Invariant mass distribution of jet and the reconstructed $\tilde{\chi}_2^0$ for m_0= 300 GeV, $m_{1/2}$= 150 GeV and tan β=2. Dotted line shows combinatorial background.
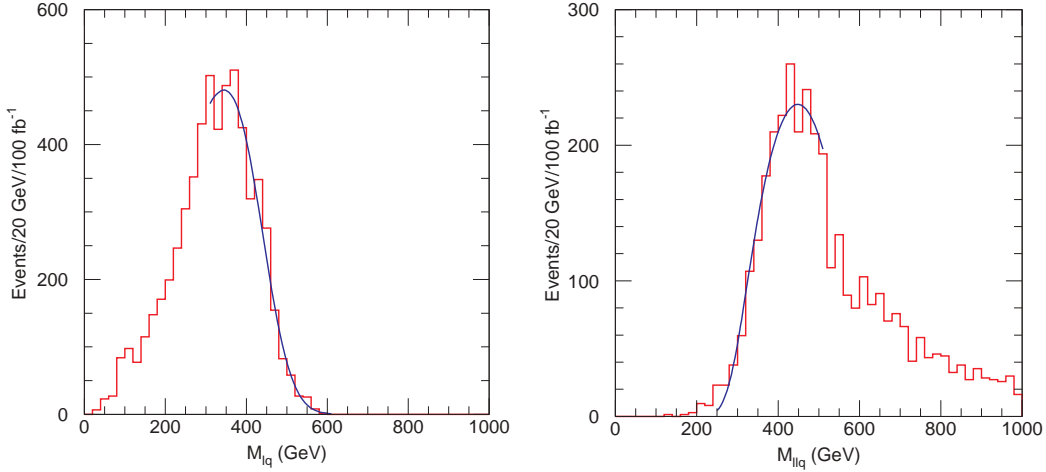
Figure 20: Invariant mass distributions of qℓ and q$\ell\ell$ (at LHC point 5).

unknown masses can be determined model-independently. Although errors of these determined masses are strongly correlated, accuracies of these masses are 3, 6, 9 and 12% for $m(\tilde{q}_L), m(\tilde{\chi}_2^0), m(\tilde{\ell}^\pm)$ and $m(\tilde{\chi}_1^0)$, respectively. We can examine SUSY model using the model-independent measurement [27]. Furthermore, there is one more constraint from A$_{\ell\ell}$ defined in eq.(2). Thus four unknown masses can be fitted with five constraints(1C fit) for this 2-body decay chain.

Following decay chains of $\tilde{g}$ is used to obtain an information about $\tilde{g}$ mass.

$\tilde{g} \rightarrow \tilde{\chi}_2^0 q\bar{q}$
$\qquad \rightarrow \ell\ell\tilde{\chi}_1^0$
$\quad \rightarrow \tilde{\chi}_1^\pm q\bar{q}$
$\qquad \rightarrow \ell\nu\tilde{\chi}_1^0$

Four high p_T jets and three leptons are required to select $\tilde{g}\tilde{g}$ events. Figure 21 shows the invariant mass distribution of two high p_T jets. Since $\tilde{\chi}_2^0$ and $\tilde{\chi}_1^\pm$ are almost always nearly degenerate [13], the end point of M$_{jj}$ is observed at the mass difference between $\tilde{g}$ and $\tilde{\chi}_2^0/\tilde{\chi}_1^\pm$. This can be determined with an accuracy of 1.5%. Main systematic error comes from uncertainty of calibration of jet energy scale (1%). Three masses of $\tilde{g}, \tilde{\chi}_2^0(\tilde{\chi}_1^\pm)$ and $\tilde{\chi}_1^0$ can be determined assuming the relation between $m(\tilde{\chi}_1^0)$ and $m(\tilde{\chi}_2^0)$.

Dominant decay mode of $\tilde{q}_R$ is $\tilde{q}_R \rightarrow q\tilde{\chi}_1^0$. Kinematic end point of p_T distribution of the highest p_T-jet is related to $m(\tilde{q}_R)$, since p_T^{max} is proportional to $\frac{1}{2}m(\tilde{q}_R)(1 - (m(\tilde{\chi}_1^0)/m(\tilde{q}_R))^2)$ in $\tilde{q}_R$ rest-frame, and since $(m(\tilde{\chi}_1^0)/m(\tilde{q}_R))^2$ is expected to be small. $m(\tilde{q}_R)$ can be determined with an accuracy of a few %.

Min$(m(\tilde{q}), m(\tilde{g}))$ can be also determined by inclusive study. $\not{E}_T + \sum_{jets} p_T$ is proportional to min$(m(\tilde{q}_R), m(\tilde{g}))$ as shown in Fig. 22. It can be determined independently from the exclusive studies mentioned above. Accuracy is about 15% [23] including systematic errors, and large contributions comes from the uncertainty of $\not{E}_T + \sum_{jets} p_T$- distribution for the background processes.

3.4 Summary and comments on mSUGRA

$\tilde{\chi}_2^0$ plays important role to determine masses of the SUSY particles, and studies has been done systematically [11,24] for various decay modes presented in table 3. $\tilde{g} \rightarrow q\bar{q}\tilde{\chi}_2^0(\tilde{\chi}_1^\pm)$ and $\tilde{q} \rightarrow q\tilde{\chi}_{1,2}^0$ processes are useful to determine $\tilde{g}$ or $\tilde{q}$ mass as presented in Sec.3.3. Although all of $\tilde{g}$-, $\tilde{q}_{L/R}$-
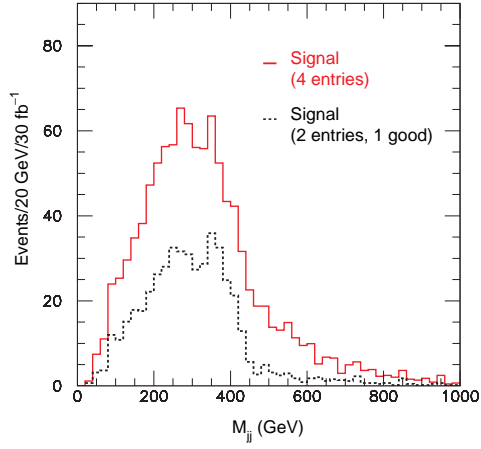
Figure 21: Invariant mass distributions of two jets (at LHC point 4). Solid line shows all combinations. Combinations of two hardest jets and two softest jets are rejected to obtained correct combinations (dotted line).
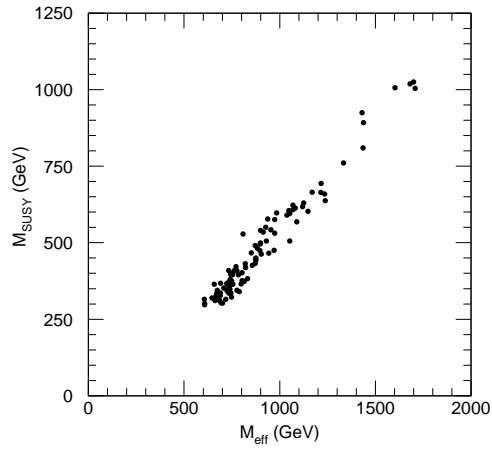

Figure 22: X-axis is fitted value of the peak of $\not{E}_T + \sum_{jets} p_T$ distribution. Y-axis is $\min(m(\tilde{q}_R), m(\tilde{g}))$. This relation is obtained in mSUGRA model.

Table 4: Determination of mSUGRA parameters (L=30 fb^{-1}): 'D' and 'ND' mean 'determined' and 'not determined',respectively.

LHC point	m_0 (GeV)	$m_{1/2}$ (GeV)	A_0 (GeV)	$\tan\beta$	$\mathrm{sign}(\mu)$
1	400±100	400±10	ND	2.0±0.08	D
2	400±100	400±10	ND	10.0±2.0	D
3	200±10	100±1	ND	2.0±0.05	D
4	800±50	200±4	ND	10.0±2.0	D with L=300 fb^{-1}
5	$100^{+4.1}_{-2.2}$	300±2.7	ND	2.0±0.1	D
6	236±37	200±14	ND	41±3.9	ND

, $\tilde{\ell}^{\pm}$-, $\tilde{\chi}_2^0$- and $\tilde{\chi}_1^0$-mass can not be determined independently, many parts of the mSUGRA parameters can be determined [11] by global fit using these measurements on these end points, since there are strong correlations between these masses in the mSUGRA model. Fitted values of the mSUGRA parameters are summarized in table 4 for various LHC points. As mentioned in Sec.3.1, $m_{1/2}$ is determined mainly by m($\tilde{\chi}_2^0$) and m($\tilde{g}$), and it's error is smaller than 10%. m($\tilde{q}_L$) and m($\tilde{\ell}_R^{\pm}$) contribute to strong constraint on m_0, whose accuracy is 5-20%. $\tan\beta$ is determined by Higgs boson mass.

When $|\mu|$ mass is not larger than wino mass ($\sim 0.8 m_{1/2}$), the heavier states of chargino and neutralino also appear in the cascade decay chain of $\tilde{q}$ and $\tilde{g}$. Substantial branching fraction including $\tilde{\chi}_2^{\pm}$ and $\tilde{\chi}_4^0$;

$$\tilde{q} \to \tilde{\chi}_2^{\pm}/\tilde{\chi}_4^0 + q$$
$$\to \tilde{\chi}_2^0/\tilde{\chi}_1^{\pm} + Z^0/W^{\pm}$$
$$\to \tilde{\chi}_1^0 + f\bar{f}$$

is expected in this case. Event topology of such a decay chain is more complicated, but it is a good chance to measure $|\mu|$ directly. $|\mu|$ is important, since Higgsino plays important role to the Electroweak symmetry breaking in Supersymmetry. It is necessary to study systematically decay chains involving $\tilde{\chi}_2^{\pm}$ and $\tilde{\chi}_4^0$.

4   Conclusions

The standard Higgs boson should be discovered at LHC within one year with just integrated luminosity of 10fb^{-1}, if it exists less than 1 TeV. We can perform a critical test on the Higgs mechanism. Vector boson fusion process plays important role for the discovery.

Supersymmetry should be discovered at LHC within one year, if $\tilde{g}$ and $\tilde{q}$ are lighter than about 2.0 TeV. Signals will be, perhaps, found not only in the ($\not{E}_T$ + jets) channel but also in ($\not{E}_T$ + jets + lepton(s)) channels. Exclusive studies have been performed. $\tilde{\chi}_2^0$ plays important role to determine masses of the SUSY particles, and studies has been done systematically. In many cases, it should be possible to measure many combinations of masses of SUSY particles from various kinematic distributions. Masses of $\tilde{g}$, $\tilde{q}$, $\tilde{\ell}^{\pm}$, $\tilde{\chi}_2^0$ and $\tilde{\chi}_1^0$ can be determined with help of model. Accuracies of these masses are about a few–10%. When there are at least three 2-body decay chain, masses can be determined model-independently.

References

1. http://lhc.web.cern.ch/lhc/
2. ATLAS Technical proposal, CERN/LHCC/94-43.

3. CMS Technical proposal, CERN/LHCC/94-38.
4. ATLAS Physics TDR vol.1 , CERN/LHCC/99-15.
5. http://cmsdoc.cern.ch/cms/TDR/
6. http://lepewwg.web.cern.ch/LEPEWWG/plots/winter2003/
7. M. Spira, hep-ph/9705337. There are also the detail calculations of K-factor in this reference.
8. T. Plehn, D. Rainwater and D. Zeppenfeld, Phys. Lett. **B454** (1999) 297-303.
9. A. Djouadi, J. Kalinowski and M. Spira, Comput. Phys. Commun. **108** (1998) 56-74.
10. F. Gianotti, Presented at LHCC open session 5/7/2000,
    http://atlasinfo.cern.ch/Atlas/GROUPS/PHYSICS/HIGGS/higgs-www/LHCC-talks/lhcc.pdf
11. ATLAS Physics TDR vol.2 , CERN/LHCC/99-15.
12. S. Asai et al., Eur. Phys. J. direct s2003-01-010-8.
13. General Reviews: H.P. Nilles, Phys. Rep. **110** (1984) 1
    H.E. Haber and G.L. Kane, Phys. Rep. **117** (1985) 75.
14. General Reviews: G. Jungman, M. kamionkowski and K. Griest, Phys. Rept. **267** (1996) 195.
15. S. Abel et al., hep-ph/0003154 for review
    L. Alvarez-Gaume, J. Polchinski and M.B. Wise, Nucl. Phys. **B221** (1983) 495
    L. Ibanez, Phys. Lett. **B118** (1982) 73
    J. Ellis, D.V. Nanopolous and K.Tamvakis, Phys. Lett. **B121** (1983) 123.
16. M. Dine, W. Fischler and M. Srednicki, Nucl. Phys. **B189** (1981) 575
    S. Dimopoulos and S. Raby, Nucl. Phys. **B192** (1981) 353
    C. Nappi and B. Ovrut, Phys. Lett. **B113** 175
    L. Alvarez-Gaume, M. Claudson and M.B. Wise, Nucl. Phys. **B207** (1982) 961
    M. Dine and A.E. Nelson, Phys. Rev. **D48** (1993) 1227
    M. Dine, A.E. Nelson and Y. Shirman, Phys. Rev. **D51** (1995) 1362
    M. Dine et al., Phys. Rev. **D53** (1996) 2658.
17. P. Fayet, Phys. Lett. **B69** (1977) 489.
18. M. Drees and K. Hikasa, Phys. Lett. **B252** (1990) 127
    K. Hikasa and M. Kobayashi, Phys. Rev. **D36** (1987) 724
    A. Bartl, W. Majerotto and W. Porod, Z. Phys. **C64** (1994) 499.
19. E. Eichten et al., Rev. Mod. Phys. **56** (1984) 579.
20. M. Spira, Nucl. Phys. Proc. Suppl. **89** (2000) 222.
21. H. Baer, F.E. Paige, S.D. Protopopescu and X. Tata, hep-ph/0001086 (2000).
22. S. Mrenna, Comp. Phys. Comm. **101** (1997) 232
    T. Sjöstrand, Comp. Phys. Comm. **82** (1994) 74.
23. D.R. Tovey, Phys. Lett. **B498** (2001) 1.
24. S. Abdullin et al., CMS/Note/98-006, hep-ph/9806366.
25. M. Nojiri, D. Toya, and T. Kobayashi, Phys. Rev. **D62** (2000) 075009.
26. By A. Djouadi, Y. Mambrini and M. Muhlleitner Eur. Phys. J. **C20** (2001) 563.
27. B.C. Allanach, C.G. Lester, M.A. Parker and B.R. Webber CERN-TH-2000-149 (2000).